

## Article

# Rapid Microwave-Assisted Synthesis of Fe<sub>3</sub>O<sub>4</sub>/SiO<sub>2</sub>/TiO<sub>2</sub> Core-2-Layer-Shell Nanocomposite for Photocatalytic Degradation of Ciprofloxacin

Ivana Gabelica <sup>1,\*</sup>, Lidija Ćurković <sup>1,\*</sup>, Vilko Mandić <sup>2,\*</sup>, Ivana Panžić <sup>2</sup>, Davor Ljubas <sup>1</sup> and Krešo Zadro <sup>3</sup>

<sup>1</sup> Faculty of Mechanical Engineering and Naval Architecture, University of Zagreb, 10000 Zagreb, Croatia; davor.ljubas@fsb.hr

<sup>2</sup> Faculty of Chemical Engineering and Technology, University of Zagreb, 10000 Zagreb, Croatia; ipanzic@fkit.hr

<sup>3</sup> Faculty of Natural Sciences, University of Zagreb, 10000 Zagreb, Croatia; kzadro@phy.hr

\* Correspondence: ivana.gabelica@fsb.hr (I.G.); lidija.curkovic@fsb.hr (L.Ć.); vmandic@fkit.hr (V.M.)

**Abstract:** In this work, magnetic nanoparticles based on magnetite were successfully prepared via rapid microwave-assisted synthesis. In order to obtain the ternary core-shell Fe<sub>3</sub>O<sub>4</sub>/SiO<sub>2</sub>/TiO<sub>2</sub> nanocomposite, first magnetite (Fe<sub>3</sub>O<sub>4</sub>) nanoparticles were coated with a protective layer of silica (SiO<sub>2</sub>) and finally with titania (TiO<sub>2</sub>). The composite configuration comprising porous and photoactive shells should facilitate the removal of organic micropollutants (OMPs) from water. Furthermore, the magnetic core is critical for processing the management of the photocatalytic powder suspension. The magnetization of the prepared magnetic nanoparticles was confirmed by vibrating-sample magnetometry (VSM), while the structure and morphology of the core-shell nanocomposite were investigated by means of XRD, FTIR, and SEM. Adsorption and photocatalysis were evaluated by investigating the removal efficiency of ciprofloxacin (CIP) as a model OMP using the prepared magnetic core-shell nanocomposite under UV-A light irradiation. It was found that the Fe<sub>3</sub>O<sub>4</sub>/SiO<sub>2</sub>/TiO<sub>2</sub> nanocomposite showed good synergistic adsorption and photocatalytic properties. The measurement of iron in eluate confirmed that no leaching occurred during the photocatalytic examination. The recovery of magnetic nanocomposite by an external magnetic field confirmed that the magnetically separated catalyst is highly suitable for recycling and reuse.

**Keywords:** microwave synthesis; magnetite; silica; titania; core-shell nanocomposite



**Citation:** Gabelica, I.; Ćurković, L.; Mandić, V.; Panžić, I.; Ljubas, D.; Zadro, K. Rapid Microwave-Assisted Synthesis of Fe<sub>3</sub>O<sub>4</sub>/SiO<sub>2</sub>/TiO<sub>2</sub> Core-2-Layer-Shell Nanocomposite for Photocatalytic Degradation of Ciprofloxacin. *Catalysts* **2021**, *11*, 1136. <https://doi.org/10.3390/catal11101136>

Academic Editors: Laura Bergamonti and Pier Paolo Lottici

Received: 20 August 2021

Accepted: 20 September 2021

Published: 22 September 2021

**Publisher's Note:** MDPI stays neutral with regard to jurisdictional claims in published maps and institutional affiliations.



**Copyright:** © 2021 by the authors. Licensee MDPI, Basel, Switzerland. This article is an open access article distributed under the terms and conditions of the Creative Commons Attribution (CC BY) license (<https://creativecommons.org/licenses/by/4.0/>).

## 1. Introduction

Magnetic nanomaterials have been getting a lot of attention lately due to their specific physical properties and various applications in medicine and biomedicine. Another important application lies in the area of supports for photocatalysts in advanced oxidation processes for the degradation of organic micropollutants (OMPs).

Due to their various applications and specific physical properties, magnetic nanomaterials are a constant topic of scientific research. Magnetic properties of materials change significantly, when the size of each particle is reduced to nanoscale compared to those of bulk materials [1]. Therefore, by having uniformly sized magnetic nanoparticles (such as magnetite), one can enable a facile separation process, i.e., extraction of the magnetic nanoparticles from a solution using an external magnetic field. Magnetite is one of the most famous iron oxides with inverse spinel structure B(AB)O<sub>4</sub>. A and B ions in parentheses occupy octahedral sites, while the rest of the B ions occupy tetrahedral sites [2]; thus, magnetite shows ferrimagnetic ordering. However, when the size of each particle is reduced to nanoscale, precisely between 15 and 20 nm, the particles will exhibit magnetic moment as a single domain under an external magnetic field which behaves as a superparamagnet [3], whereas in the absence of a magnetic field they will have zero

average residual magnetization, and more precisely, their magnetization disappears [4]. In that case, magnetic behavior is determined by the magnetic anisotropy energy of each particle and the magnetic dipole–dipole interaction between the particles. For the particle to exhibit superparamagnetic behavior, the magnetic anisotropy energy must be greater than that of the dipole–dipole interaction [1]. This behavior allows the fast, easy, reversible and selective magnetic separation of the particles from a solution using an external magnetic field. The use of magnetite nanoparticles is advantageous because of their non-toxicity and low cost compared to other magnetic nanoparticles such as nickel and cobalt [5,6]. Consequently, magnetite nanoparticles have found applications such as drug delivery systems [7], magnetic imaging [8], magnetic resonance imaging (MRI) [9], magnetic hyperthermia applications [10], heavy metal detection [11], lithium-ion batteries [12], and antibacterial activities [13]. Photocatalytically, magnetic nanoparticles have been used in various configurations such as supports of photocatalysts for the photodegradation of various dyes [14–18], natural organic matter in water [19], herbicides in wastewater [20], the treatment of drinking water [21], and the removal of pharmaceuticals [22–24].

Magnetic nanoparticles can be synthesized using various physical methods such as gas-phase deposition, electron beam lithography, pulsed laser ablation, laser-induced pyrolysis, power ball milling, combustion, and chemical methods including co-precipitation, thermal decomposition, reverse microemulsion, and hydrothermal, solvothermal, and lately microwave-assisted synthesis [3]. Each of the abovementioned methods shows some limitations in either complexity, modularity, processing price, or yield homogeneity, while comparatively the microwave-assisted synthesis may offer a simple, variable, cheap and fast alternative synthetic route. The microwave-assisted synthesis is based upon the interaction of microwaves with the material, and more precisely, molecules with a dipole moment absorb microwaves and thereby transform energy to heat which is generated within the material or suspension itself. The temperature gradient in microwave synthesis is therefore opposite to that in conventional heating, i.e., from the inside out, the so-called in-core heating. Microwave heat transfer depends on the specific loss factor characteristic for each solvent. The higher this value, the better the solvent will absorb microwaves [25,26]. During synthesis, high energy output enables high heating rates and high product yields, but also a precise heating control, all of which enable rapid phase formation with a monodisperse particle size distribution [27,28]. Shorter synthesis time is also enabled by the superheating phenomenon, in which the solvent when exposed to microwaves in a closed reactor can be heated to temperatures above the atmospheric boiling point without boiling [29].

Magnetite nanoparticles are not particularly photoactive; therefore, for their use in advanced oxidation processes (AOPs), a photocatalytic semiconductor is necessary. Due to its superior photocatalytic activity, low price, good chemical stability, and non-toxicity, TiO<sub>2</sub> is one of the most common and well-known semiconductors. Chemical reactions on a TiO<sub>2</sub> surface are induced by the absorption of photons from a light source, with a wavelength below 400 nm. The absorption of light causes the promotion of electron (e<sup>-</sup>) from the valence band to the conduction band, which generates a hole (h<sup>+</sup>) in the valence band of the photocatalyst. Photocatalytic activity can be further improved by adding various electron scavengers, which react with electrons and prevent the recombination of electron–hole pairs, thus enabling the formation of different radicals which degrade pollutants [30]. Balayeva et al. [31] and Yu et al. [32] developed a new visible-light-sensitive photocatalyst based on TiO<sub>2</sub>. TiO<sub>2</sub> as a photocatalyst can be used in the form of TiO<sub>2</sub> powder suspension, or it can be immobilized by different techniques on various substrates [29,33,34]. The main problem of photocatalyst application in the form of a suspension is their separation from the treated water [35]. One way of the immobilization of TiO<sub>2</sub> is the deposition of the TiO<sub>2</sub> shell on the magnetite core, which allows the separation of the photocatalyst by an external magnet from the treated water. A sol-gel route is an established chemical route that can be easily utilized for the deposition of titania [29]. A similar sol-gel process can be used to derive another shell layer [14], in this case a protective silica shell layer. It has been reported that, in the case of the direct contact between iron oxide and TiO<sub>2</sub>, an electron

transfer from titania to iron oxide occurs which causes phase separation and consequently the leaching of iron [12,28]. In order to prevent the unwanted iron leaching, inserting a buffer-protective silica shell layer between the magnetite core and the outer titania shell should mitigate the mentioned electron transfer.

Some photocatalysts have also shown favorable adsorption behavior in addition to photocatalytic degradation performance, for example in the case of rhodamine dye degradation by  $\text{BiVO}_4$  [36], remazol brilliant blue dye by  $\text{N-TiO}_2$  [37], methylene blue by the ternary  $\text{MgFe}_2\text{O}_4\text{-TiO}_2\text{NPs@GO}$  nanocomposite [38], ciprofloxacin (CIP) by the ternary  $\text{BiOCl/CQDs/rGO}$  photocatalyst [39], and methyl orange by nano-heterostructure  $\text{CTS@C}$  [40]. According to the available literature, the adsorption and photocatalytic behavior of the core-shell  $\text{Fe}_3\text{O}_4/\text{SiO}_2/\text{TiO}_2$  nanocomposite, with respect to the possible synergistic performance, has not been investigated so far. Therefore, in the present work, the microwave-assisted synthesis, characterization, adsorption, and photocatalytic properties of this core-shell nanocomposite were studied. CIP was used as a model micropollutant from the class of quinolone antibiotics. The degradation data were fitted with kinetic models to explain the mechanism of adsorption.

## 2. Results and Discussion

### 2.1. Characterisation of Core-Shell $\text{Fe}_3\text{O}_4/\text{SiO}_2/\text{TiO}_2$ Nanoparticles

Figure 1 shows the FTIR spectra for  $\text{Fe}_3\text{O}_4$ ,  $\text{Fe}_3\text{O}_4/\text{SiO}_2$ , and  $\text{Fe}_3\text{O}_4/\text{SiO}_2/\text{TiO}_2$  nanoparticles synthesized at 100 °C (Figure 1a), 150 °C (Figure 1b), and 200 °C (Figure 1c) by the microwave-assisted method. Additionally, Figure 1d shows the FTIR spectra of pure  $\text{TiO}_2$  and  $\text{SiO}_2$  as a reference.

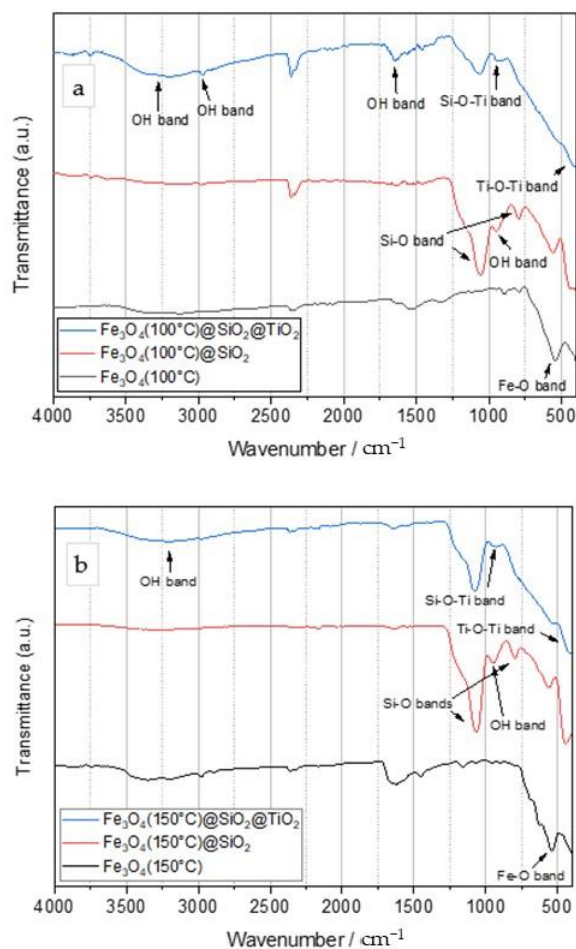
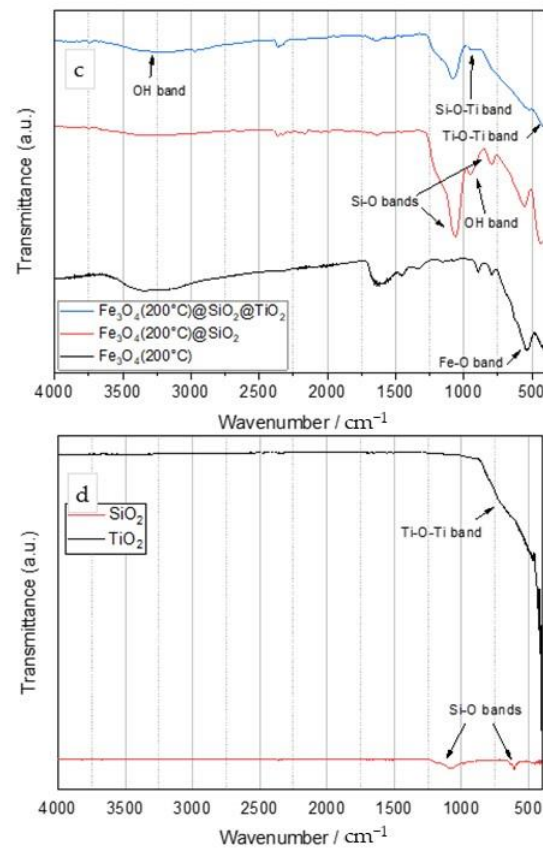


Figure 1. Cont.



**Figure 1.** FTIR spectra of  $\text{Fe}_3\text{O}_4$  (black line),  $\text{Fe}_3\text{O}_4/\text{SiO}_2$  (red line), and  $\text{Fe}_3\text{O}_4/\text{SiO}_2/\text{TiO}_2$  (blue line) particles synthesized by the microwave-assisted method at 100 °C (a), 150 °C (b), and 200 °C (c). (d) FTIR spectra of pure  $\text{TiO}_2$  and  $\text{SiO}_2$ .

The main band for magnetite nanoparticles was observed at around  $550\text{ cm}^{-1}$  and was assigned to the Fe–O stretching vibration [1]. The FTIR spectra of  $\text{Fe}_3\text{O}_4/\text{SiO}_2$  particles showed an absorption band around  $1100\text{ cm}^{-1}$ , which was assigned to the Si–O–Si asymmetric stretching vibration. The band around  $800\text{ cm}^{-1}$  originated from the deformation vibration of Si–O bonds [30], while the band at  $950\text{ cm}^{-1}$  was assigned to the asymmetric bending and stretching vibration of Si–OH [41]. The  $\text{Fe}_3\text{O}_4/\text{SiO}_2/\text{TiO}_2$  FTIR spectra showed several bands. The band around  $400\text{--}450\text{ cm}^{-1}$  was due to the stretching vibration of Ti–O–Ti [42]. The absorption bands in the range of  $2800\text{--}3800\text{ cm}^{-1}$  were due to the stretching vibrations of OH groups, probably from adsorbed water but could also be from the OH groups bonded to Si and Ti (Ti–OH and Si–OH). A small peak was observed around  $960\text{ cm}^{-1}$  and was assigned to the Si–O–Ti stretching vibration, which indicated a bond between silica and titania layers [18]. The changing of the synthesis temperature barely affected the vibration spectra of the obtained nanoparticles. Characteristic Ti–O–Ti and Si–O bands observed on the FTIR spectra of  $\text{Fe}_3\text{O}_4/\text{SiO}_2$  and  $\text{Fe}_3\text{O}_4/\text{SiO}_2/\text{TiO}_2$  nanoparticles corresponded to those of pure  $\text{SiO}_2$  and  $\text{TiO}_2$ .

The XRD analysis (Figure 2a–c) showed magnetite ( $\text{Fe}_3\text{O}_4$ ) (ICDD PDF#19-0629) as the main crystalline phase in all samples (synthesized by the microwave-assisted method at 100, 150, and 200 °C). The samples thermally treated at lower temperatures (100 °C) also showed barely noticeable traces of goethite ( $\text{FeO}(\text{OH})$ ; ICDD PDF#29-0713; highlighted with pink squares) (Figure 2a). There were no amorphous iron oxide phases or unassigned peaks. For samples with a silica coating (Figure 2b), no characteristic patterns of silica crystalline phases were observed; however, a hump centered around  $2\theta$  of  $26^\circ$  characteristic of amorphous silica was evidenced, confirming the presence of the  $\text{SiO}_2$  phase (highlighted with yellow squares). As a consequence of the silica coating, the intensity of the diffraction

signal from the magnetite phase was only slightly reduced, as the magnetite core was less available to X-rays, thereby proving the core–shell configuration of the sample. There were no additional silica amorphous phases or unassigned peaks. In the sample additionally coated with  $\text{TiO}_2$ , anatase was observed as the main phase (ICDD PDF#21-1272), magnetite is the minor phase, and the silica hump was barely visible (Figure 2c). In this case, the reduction of the diffraction signal from the magnetite phase also pointed out to the magnetite core, which was less exposed to X-rays, to the middle silica shell, which was intermediately exposed to X-rays, and the outer titania shell, readily exposed to X-rays. There were no titania amorphous phase or unassigned peaks. The synthesis temperature showed no effect on the obtained nanoparticles.

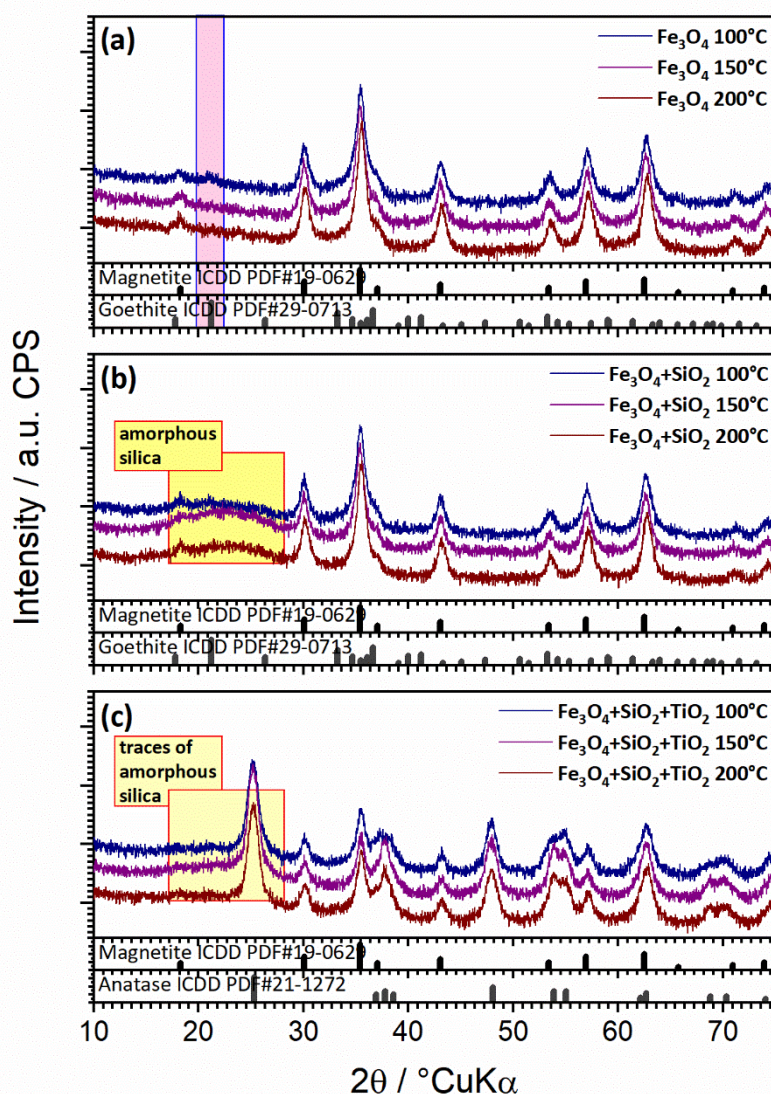


**Figure 2.** Diffractograms of  $\text{Fe}_3\text{O}_4$  (a),  $\text{Fe}_3\text{O}_4/\text{SiO}_2$  (b), and  $\text{Fe}_3\text{O}_4/\text{SiO}_2/\text{TiO}_2$  (c) samples synthesized by the microwave-assisted method at 100 °C (blue line), 150 °C (violet line), and 200 °C (brown line).

Diffraction results are in agreement with the FTIR results and confirmed the successful synthesis of the  $\text{Fe}_3\text{O}_4/\text{SiO}_2/\text{TiO}_2$  nanocomposites but additionally pointed out a two-layer core–shell configuration.

The magnetization measurements were conducted at room temperature and are shown in Figure 3. The magnetization curves showed that the obtained particles exhibited superparamagnetic behavior. The values of saturation magnetization amounted to 59, 35, and 17  $\text{emu g}^{-1}$  for  $\text{Fe}_3\text{O}_4$ ,  $\text{Fe}_3\text{O}_4/\text{SiO}_2$ , and  $\text{Fe}_3\text{O}_4/\text{SiO}_2/\text{TiO}_2$  nanoparticles, respectively. The addition of  $\text{SiO}_2$  and  $\text{TiO}_2$  layers reduced the saturation magnetization; however, it was

still enough to remove the particles from the suspension by an external magnetic field. The samples synthesized at 100 °C showed the highest values of saturation magnetization and were thus chosen for further photocatalytic experiments.

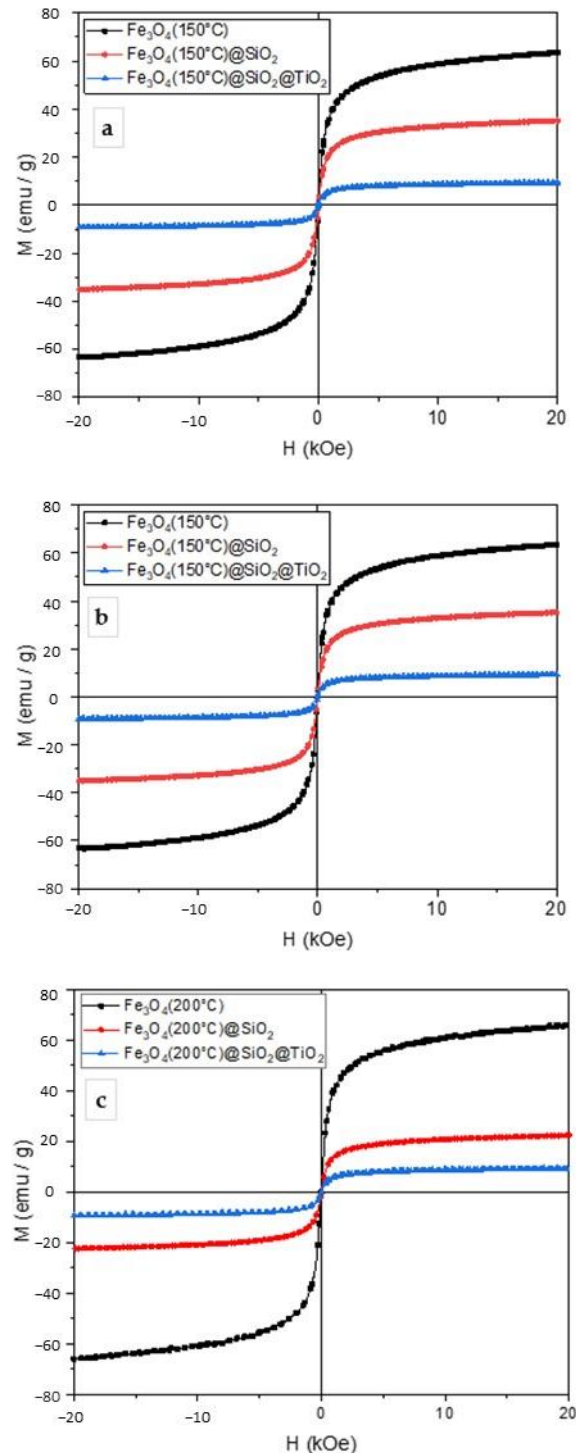


**Figure 3.** Magnetization curves of  $\text{Fe}_3\text{O}_4$ ,  $\text{Fe}_3\text{O}_4/\text{SiO}_2$ , and  $\text{Fe}_3\text{O}_4/\text{SiO}_2/\text{TiO}_2$  nanoparticles synthesized by the microwave-assisted method at 100 °C (a), 150 °C (b), and 200 °C (c).

The texture and morphology of the core-shell nanocomposites were investigated using SEM analysis with different magnifications, shown in Figure 4. The magnetite nanoparticles, shown in Figure 4a–c, had a disordered surface texture. The presence of agglomerates was due to the small size of particles and their magnetization. The surface displayed rather

low surface roughness compared to the particles coated with a layer of  $\text{SiO}_2$ , shown in Figure 4d–f. The  $\text{SiO}_2$  layer seemed to have another role in the process of manufacturing the nanocomposites, and it controlled the particle size and shape, which can be seen in the form of regularly shaped round particles in Figure 4d. The round particles were obtained with the synthesis temperature of 100 °C. The  $\text{Fe}_3\text{O}_4/\text{SiO}_2/\text{TiO}_2$  nanocomposite seemed to have a porous microstructure, which can enhance photocatalytic efficiency. However, the presence of agglomerates might reduce the active surface. To address agglomeration issues, the use of a surfactant and a longer microwave irradiation with high stirring rates may be beneficial [43–45].

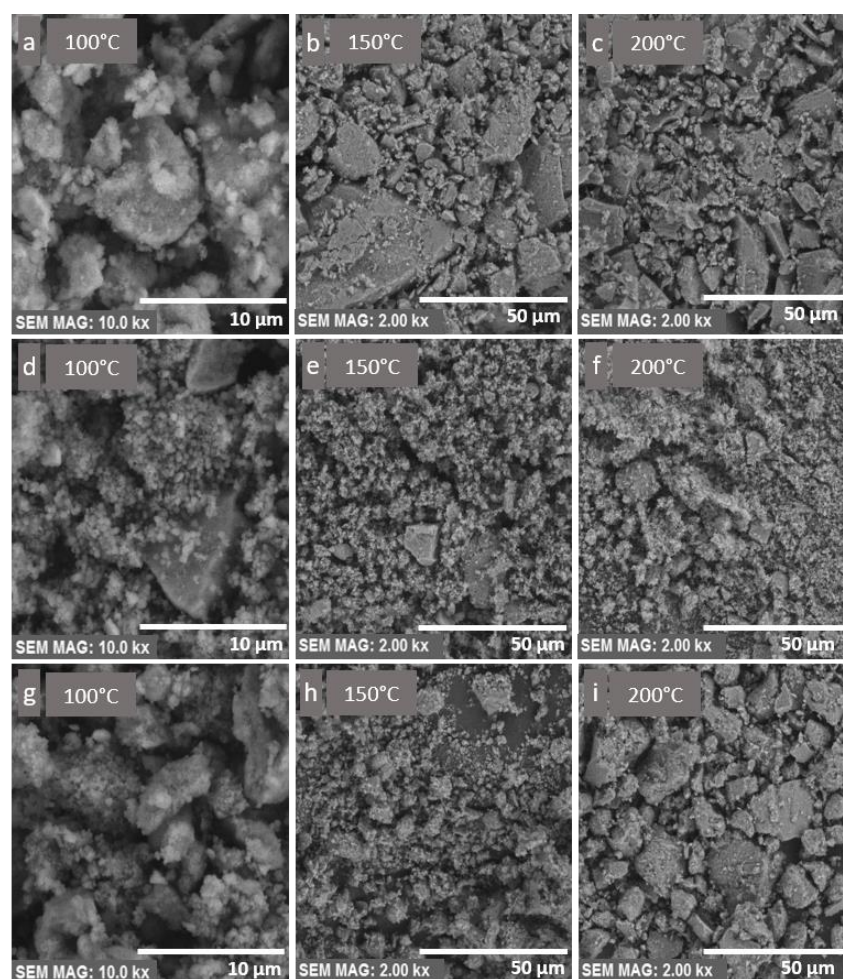


**Figure 4.** (a–c) SEM images of  $\text{Fe}_3\text{O}_4$  nanocomposites synthesized by the microwave-assisted method at 100, 150, and 200 °C, respectively. (d–f) SEM images of  $\text{Fe}_3\text{O}_4/\text{SiO}_2$  nanocomposites synthesized by the microwave-assisted method at 100, 150, and 200 °C, respectively. (g–i) SEM images of  $\text{Fe}_3\text{O}_4/\text{SiO}_2/\text{TiO}_2$  nanocomposites synthesized by the microwave-assisted method at 100, 150, and 200 °C, respectively.

## 2.2. Synergetic Effects of Adsorption and Photocatalysis

### 2.2.1. Adsorption Kinetic Studies

Prior to the photocatalytic degradation of CIP in an aqueous solution, adsorption tests were conducted to evaluate the adsorption kinetics [39,40]. The obtained results after 120 min of stirring in the dark with the synthesized photocatalyst are shown in

Figure 5. The percentage of adsorption efficiency of the  $\text{Fe}_3\text{O}_4/\text{SiO}_2/\text{TiO}_2$  nanocomposite was calculated using the equation:

$$\eta, \% = \frac{C_0 - C_t}{C_0} \times 100, \quad (1)$$

where  $\eta$  is the percentage of adsorption efficiency,  $C_0$  ( $\text{mg dm}^{-3}$ ) is the initial CIP concentration before adsorption, and  $C_t$  ( $\text{mg dm}^{-3}$ ) is the concentration of CIP at time  $t$  (min) of adsorption. It can be seen that the adsorption/desorption equilibrium was established within 30 min, with 56% of CIP adsorbed on the photocatalyst surface. Therefore, the adsorption process kinetics and mechanisms were analyzed.

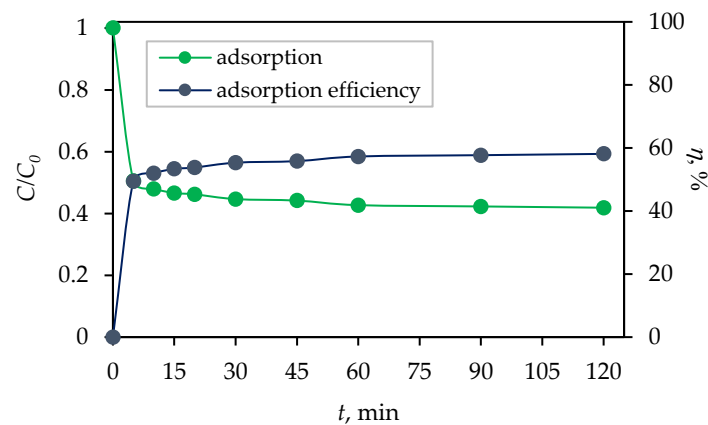


**Figure 5.** Dark adsorption and adsorption efficiency ( $\eta$ ; %) of ciprofloxacin (CIP) by  $\text{Fe}_3\text{O}_4/\text{SiO}_2/\text{TiO}_2$  nanocomposites synthesized at  $100^\circ\text{C}$  as a function of time ( $c$  (CIP) =  $10 \text{ mg dm}^{-3}$ ,  $V$  (CIP) =  $100 \text{ cm}^3$ ,  $m$  (core-shell photocatalyst) =  $50 \text{ mg}$ , and  $T = 25^\circ\text{C}$ ).

In order to yield further information about the mechanisms involved, the adsorption kinetics data were fitted with several model equations presented in the following sections, namely the Lagergren pseudo-first-order model and Ho's pseudo-second-order kinetic model, the Weber–Morris intraparticle diffusion, and the Boyd plot film diffusion models [46].

The kinetics of the CIP adsorption was investigated by applying pseudo-first-order and pseudo-second-order models. The Lagergren pseudo-first-order model is described by the following equation [47]:

$$\frac{dq_t}{dt} = k_1(q_e - q_t), \quad (2)$$

where  $q_e$  and  $q_t$  are the amounts of CIP ( $\text{mg g}^{-1}$ ) adsorbed on the  $\text{Fe}_3\text{O}_4/\text{SiO}_2/\text{TiO}_2$  nanocomposite at equilibrium and at time  $t$ , respectively, while  $k_1$  ( $\text{min}^{-1}$ ) is the rate constant of the pseudo-first-order sorption. Upon integrating with the initial conditions of  $q = 0$  when  $t = 0$ , Equation (3) yields:

$$q = q_e(1 - \exp(-kt)). \quad (3)$$

Its linearized form is written as:

$$\ln(q_e - q_t) = \ln q_e - k_1 t. \quad (4)$$

The plotting (Figure 6a) of  $\ln(q_e - q_t)$  against  $t$  gave  $q_e = \exp(\text{intercept})$  and  $k_1 = -(\text{slope})$ .

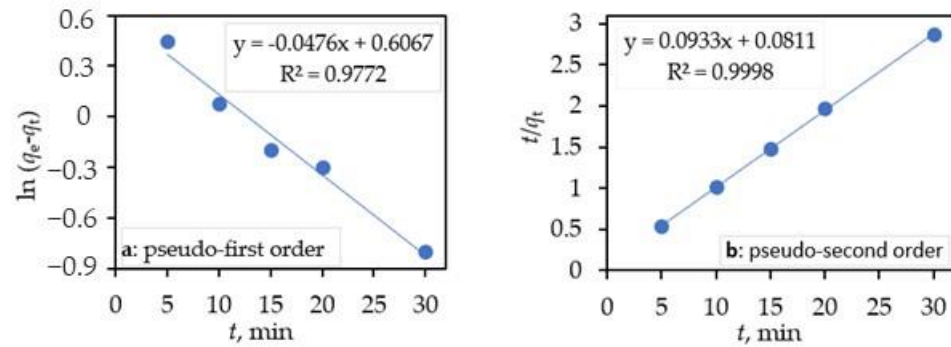


**Figure 6.** Pseudo-first-order plots (a) and pseudo-second order plot (b) of the adsorption of CIP on the ternary core–shell  $\text{Fe}_3\text{O}_4/\text{SiO}_2/\text{TiO}_2$  nanocomposite ( $c$  (CIP) =  $10 \text{ mg dm}^{-3}$ ,  $V$  (CIP) =  $100 \text{ cm}^3$ ,  $m$  (core–shell photocatalyst) =  $50 \text{ mg}$ , and  $T = 25 \text{ }^\circ\text{C}$ ).

The kinetic data were further analyzed using Ho’s pseudo-second-order kinetic model. This model assumes that the uptake rate is second-order with respect to the available surface sites [48]. The pseudo-second-order equation [49] is represented as:

$$\frac{dq_t}{dt} = k_2(q_e - q_t)^2, \quad (5)$$

where  $q_e$  and  $q_t$  are the amounts of CIP ( $\text{mg g}^{-1}$ ) adsorbed on the  $\text{Fe}_3\text{O}_4/\text{SiO}_2/\text{TiO}_2$  nanocomposite at equilibrium and at time  $t$ , respectively, while  $k_2$  is the rate constant of pseudo-second-order adsorption ( $\text{mg g}^{-1} \text{ min}^{-1}$ ). Integrating Equation (5) with the initial conditions of  $q = 0$  when  $t = 0$  and subsequent rearrangement obtains the linearized form:

$$\frac{t}{q_t} = \frac{1}{k_2 q_e^2} + \frac{t}{q_e}. \quad (6)$$

A plot (Figure 6b) of  $t/q_t$  against  $t$  gave  $1/q_e$  as the slope and  $1/k_2 q_e^2$  as the intercept. The values of  $q_e$ ,  $k_1$ , and  $R^2$  obtained after the linear plots of Equation (4) and  $q_e$ ,  $k_2$ , and  $R^2$  from the plots of Equation (6) for the CIP adsorption on the ternary core/shell  $\text{Fe}_3\text{O}_4/\text{SiO}_2/\text{TiO}_2$  nanocomposite are reported in Table 1.

**Table 1.** The pseudo-first-order and pseudo-second-order sorption models constants of CIP on the ternary core–shell  $\text{Fe}_3\text{O}_4/\text{SiO}_2/\text{TiO}_2$  nanocomposite.

$q_{e,exp}$ ( $\text{mg g}^{-1}$ )	Kinetic Model					
	Pseudo-First-Order			Pseudo-Second-Order		
	$k_1$ ( $\text{min}^{-1}$ )	$q_{e,cal}$ ( $\text{mg g}^{-1}$ )	$R^2$	$k_2$ ( $\text{g mg}^{-1} \text{ min}^{-1}$ )	$q_{e,cal}$ ( $\text{mg g}^{-1}$ )	$R^2$
10.91	0.0476	1.83	0.9772	0.107	10.72	0.9998

It can be seen (Table 1) that for a pseudo-first-order model, the linear correlation coefficient ( $R^2$ ) was lower than the pseudo-second-order correlation coefficient ( $R^2$ ). The correlation coefficients for the pseudo-second-order kinetic model was very high ( $R^2 > 0.99$ ), and the theoretical  $q_{e,cal}$  values were closer to the experimental  $q_{e,exp}$  values at the studied initial CIP concentration. This suggests that the adsorption of CIP on the ternary core/shell  $\text{Fe}_3\text{O}_4/\text{SiO}_2/\text{TiO}_2$  nanocomposite might be controlled by the second-order model.

### 2.2.2. Sorption Mechanism—Intraparticle Diffusion Model

The two kinetic models listed above could not definitely reveal the adsorption mechanism as well as the rate controlling steps in the sorption process. Thus, the intraparticle diffusion model according to Weber and Morris [50] was further applied in the present study. The intraparticle diffusion equation is expressed as:

$$q_t = k_{pi}\sqrt{t} + C_i, \quad (7)$$

where  $k_{pi}$  ( $\text{mg g}^{-1} \text{min}^{1/2}$ ) is the rate parameter of stage I and is obtained from the slope of the straight line of  $q_t$  versus  $t^{1/2}$ ;  $C_i$ , the intercept of stage  $i$ , gives an idea about the thickness of boundary layer, i.e., the larger the intercept, the greater the boundary layer effect. If intraparticle diffusion occurs, then  $q_t$  versus  $t^{1/2}$  will be linear, and if the plot passes through the origin, then the rate limiting process is only due to the intraparticle diffusion. Otherwise, some other mechanism along with intraparticle diffusion is also involved. For an adsorbate/adsorbent adsorption process, the adsorbate transfer may include the step of either external mass transfer (film diffusion) or intraparticle diffusion, or both. The intraparticle diffusion plots of  $q_t$  against  $t^{1/2}$  (Figure 7a) consisted of three linear sections with different multi-linear sections, including three linear sections with different slopes, which indicates that multiple steps take place during the sorption process [51].

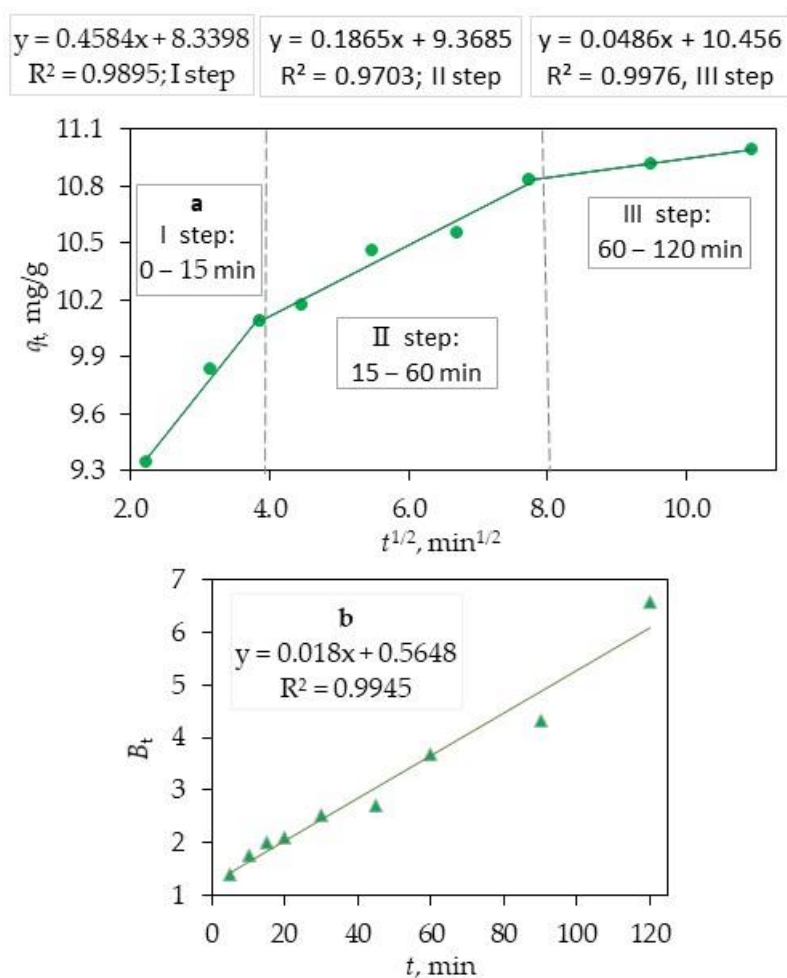


**Figure 7.** The adsorption kinetic data of CIP on the ternary core-shell  $\text{Fe}_3\text{O}_4/\text{SiO}_2/\text{TiO}_2$  nanocomposite fitted with Webe–Morris intraparticle diffusion (a) and Boyd diffusion models (b).

The first stage of sorption (the section of the curve with a large slope) corresponds to the transport of adsorbate, CIP from the bulk solution to the external surface of adsorbent, and ternary Fe<sub>3</sub>O<sub>4</sub>/SiO<sub>2</sub>/TiO<sub>2</sub> nanocomposite by film diffusion, which is also called outer diffusion (or boundary layer diffusion). The second stage of sorption describes the gradual adsorption stage, corresponding to the diffusion of the adsorbate, the ternary core-shell Fe<sub>3</sub>O<sub>4</sub>/SiO<sub>2</sub>/TiO<sub>2</sub> nanocomposite from the external surface into the pores of the adsorbent, and the ternary Fe<sub>3</sub>O<sub>4</sub>/SiO<sub>2</sub>/TiO<sub>2</sub> nanocomposite, which is called intraparticle diffusion or inner diffusion.

The third stage with a small slope indicates the final equilibrium stage. This step is considered very fast and thus cannot be treated as the rate-controlling step. Generally, the adsorption rate is controlled by outer diffusion or intra-particle diffusion or both. It is clear that the rate-controlling step of CIP adsorption on the ternary core-shell Fe<sub>3</sub>O<sub>4</sub>/SiO<sub>2</sub>/TiO<sub>2</sub> nanocomposite involves complex processes, including outer diffusion (film diffusion) and intraparticle diffusion. The model parameters obtained from the three stages of plots are listed in Table 2.

**Table 2.** Intraparticle diffusion model constants and correlation coefficients for the adsorption of CIP on the ternary Fe<sub>3</sub>O<sub>4</sub>/SiO<sub>2</sub>/TiO<sub>2</sub> nanocomposite.

Intraparticle Diffusion								
First Stage of Sorption			Second Stage of Sorption			Third Stage of Sorption		
$k_{p1}$ (mg g <sup>-1</sup> min <sup>-1/2</sup> )	$C_1$	$R^2$	$k_{p2}$ (mg g <sup>-1</sup> min <sup>-1/2</sup> )	$C_2$	$R^2$	$k_{p3}$ (mg g <sup>-1</sup> min <sup>-1/2</sup> )	$C_3$	$R^2$
0.458	8.34	0.9895	0.186	9.37	0.9703	0.0486	10.46	0.9976

Based on Table 2, the curves do not cross the origin, because the charts do not cut the zero point, so the intraparticle diffusion is not the only rate-limiting stage in this adsorption system and other mechanisms are also included. To better understand the principal mechanism for controlling the rate of the adsorption process, the Boyd diagram was used with the utilization of the following equation and the drawing of the  $B_t$  graph in terms of  $t$ . The role of controlling the rate of film diffusion and intraparticle diffusion in the mechanism of adsorption of CIP can be determined by plotting this diagram. Thus, if the linear plot of data fitting has an intercept of zero and the regression coefficient is also higher than 0.99, the intraparticle diffusion of the process stage will control the process speed; otherwise, the influence of the film will also be involved. As shown in Figure 7b, this diagram is linear but does not cross the origin, bringing to the conclusion that the inherent penetration along with the film penetration governs the adsorption.

### 2.2.3. Photocatalytic Kinetic Studies

Comparisons of results of dark adsorption [52], photolysis, and photocatalytic degradation (three replicates) of CIP are presented in Figure 8. It can be seen that the photolytic (without photocatalyst nanocomposite) degradation of CIP lowered its concentration by around 40% and dark adsorption by around 56% after 30 min, while photocatalytic degradation lowered CIP concentration by around 94% after 120 min of irradiation.

The efficiency of photocatalytic degradation ( $\eta$ ; %) of CIP by the Fe<sub>3</sub>O<sub>4</sub>/SiO<sub>2</sub>/TiO<sub>2</sub> nanocomposite synthesized at 100 °C is shown in Figure 9a. The efficiency of photocatalytic degradation was calculated according to Equation (1). It can be seen that the degradation efficiency was 94.0% after 120 min of photocatalysis under UV light.

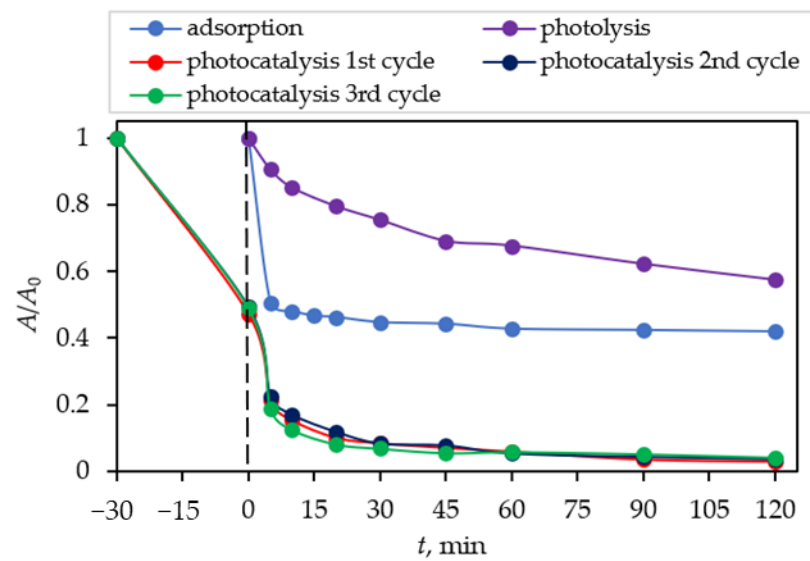


**Figure 8.** Dark adsorption and photolytic and photocatalytic degradation of CIP as a function of irradiation time by the  $\text{Fe}_3\text{O}_4/\text{SiO}_2/\text{TiO}_2$  nanocomposite synthesized at  $100^\circ\text{C}$ .

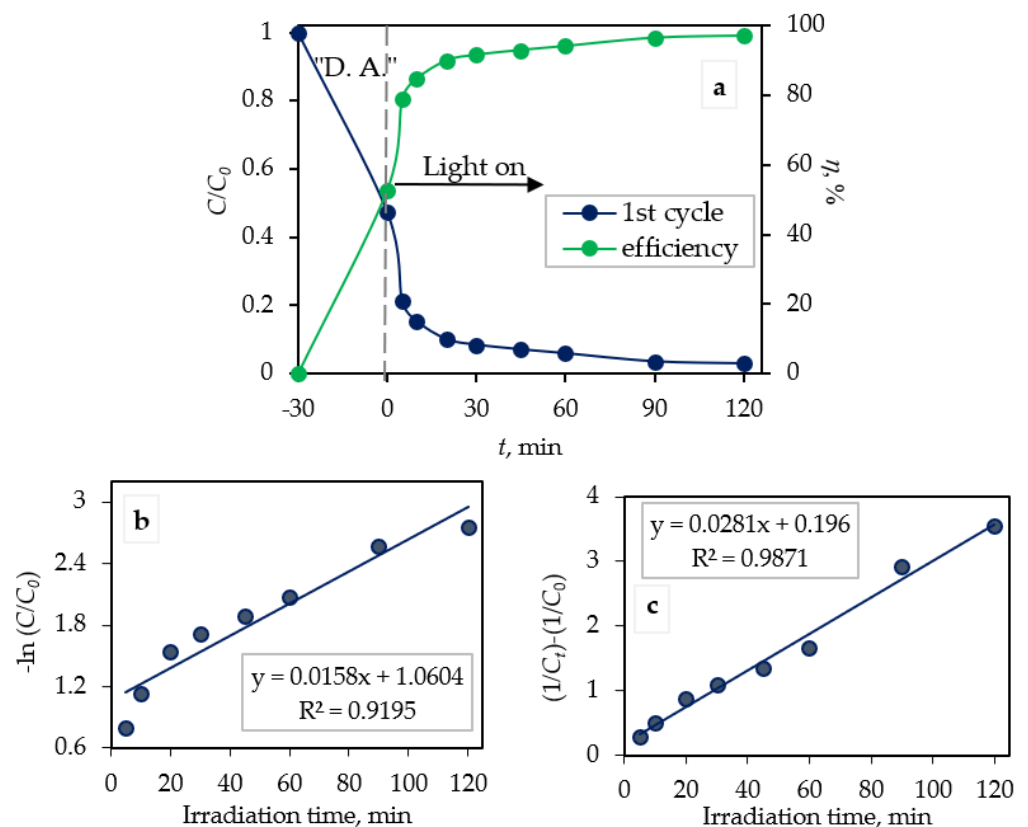


**Figure 9.** (a) Photocatalytic degradation of CIP by the  $\text{Fe}_3\text{O}_4/\text{SiO}_2/\text{TiO}_2$  nanocomposite synthesized at  $100^\circ\text{C}$  monitored via UV/VIS spectrophotometry. The pseudo-first-order plot (b) and the pseudo-second-order plot (c) of CIP photocatalytic degradation.

In order to investigate the kinetics of the photocatalytic degradation of CIP by the  $\text{Fe}_3\text{O}_4/\text{SiO}_2/\text{TiO}_2$  nanocomposite, the pseudo-first-order and pseudo-second-order kinetic models were used. The linear form of the pseudo-first-order kinetic model is described as [53]:

$$\ln \frac{C_0}{C_t} = k_1 \cdot t. \quad (8)$$

The linear form of the pseudo-second-order kinetic model is written as [53]:

$$\frac{1}{C_t} - \frac{1}{C_0} = k_2 \cdot t, \quad (9)$$

where  $C_t$  ( $\text{mg dm}^{-3}$ ) is the concentration of CIP at time  $t$  (min),  $C_0$  ( $\text{mg dm}^{-3}$ ) is the initial CIP concentration, and  $k_1$  ( $\text{min}^{-1}$ ) and  $k_2$  ( $\text{mg dm}^{-3} \text{min}^{-1}$ ) are the degradation rate constants.

The first-order degradation rate constant ( $k_1$ ) from Equation (8) can be calculated by the slope of the straight line obtained by plotting the linear regression of  $-\ln(C/C_0)$  versus irradiation time ( $t$ ) (Figure 9b). The second-order degradation rate constant ( $k_2$ ) from Equation (9) can be calculated by the slope of the straight line obtained from plotting linear regression of  $\frac{1}{C_t} - \frac{1}{C_0}$  versus irradiation time ( $t$ ) (Figure 9c). The degradation rate constants  $k_1$  and  $k_2$  were as follows:  $0.0158 \text{ min}^{-1}$  and  $0.0281 \text{ mg dm}^{-3} \text{ min}^{-1}$ . It can be seen (Figure 9a,b) that for a pseudo-first-order model, the linear correlation coefficient ( $R^2$ ) was lower (0.9195) than the pseudo-second-order correlation coefficient (0.9871). According to the obtained data, the photocatalytic degradation of CIP by the ternary core/shell  $\text{Fe}_3\text{O}_4/\text{SiO}_2/\text{TiO}_2$  nanocomposite was best fitted with pseudo-second-order kinetics.

### 2.3. Reusability and Stability of the Magnetic Ternary Core–Shell $\text{Fe}_3\text{O}_4/\text{SiO}_2/\text{TiO}_2$ Catalyst

Reusability and stability is vital for the catalyst and was confirmed by repeating the decomposition process three times (Figure 10). After three repetitions (photocatalytic degradation of three cycles), the photodegradation efficiency of CIP decreased from 94.0 (1st cycle) to 91.0% (3rd cycle). Between cycles, the magnetic nanocomposite was removed from the solution by an external magnetic field, washed and dried. The magnetic ternary core–shell  $\text{Fe}_3\text{O}_4/\text{SiO}_2/\text{TiO}_2$  catalyst featured high stability and suitable reusability under UV light irradiation.

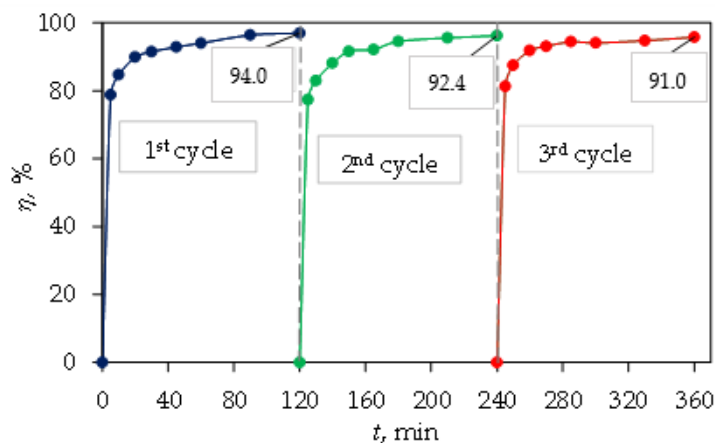


**Figure 10.** Reusability efficiencies of the ternary core–shell  $\text{Fe}_3\text{O}_4/\text{SiO}_2/\text{TiO}_2$  photocatalyst for three consecutive cycles.

The measurements of iron concentration in eluate after adsorption, photolysis, and photocatalysis tests were performed by means of atomic absorption spectroscopy and confirmed that no iron leaching occurred during the photocatalytic examination.

## 3. Materials and Methods

### 3.1. Materials

For the synthesis of magnetic nanoparticles ( $\text{Fe}_3\text{O}_4$ ), iron(III) chloride hexahydrate ( $\text{FeCl}_3 \cdot 6\text{H}_2\text{O}$ ; VWR chemicals, Germany), iron(II) sulfate heptahydrate ( $\text{FeSO}_4 \cdot 7\text{H}_2\text{O}$ ; Alfa Aesar, Kandel, Germany), sodium hydroxide ( $\text{NaOH}$ ; Grammol, Zagreb, Croatia), and deionized water (DI) were used.

For the SiO<sub>2</sub> coating, SiO<sub>2</sub> sol was prepared by mixing ethanol (EtOH, 96% p.a.; Grammol, Croatia) as the solvent and tetraethoxy silane (TEOS; Merck, Darmstadt, Germany) was used as the precursor, while ammonia (NH<sub>3</sub>, 25%; Grammol, Zagreb, Croatia) was used as the catalyst.

For the TiO<sub>2</sub> coating, TiO<sub>2</sub> sol was prepared by mixing titanium(IV) isopropoxide TIP (Sigma-Aldrich, St. Louis, MO, USA) as the precursor, 2-propanol (PrOH; Grammol, Croatia) was used as the solvent, acetylacetone (AcAc; Sigma-Aldrich, St. Louis, MO, USA) was utilized as the chelating agent, and nitric acid (HNO<sub>3</sub>; Carlo Erba Reagents, Barcelona, Spain) was employed as the catalyst.

For photocatalytic experiments CIP (98%; Acros organics, Thermo Fisher Scientific, NJ, USA) was used as the model OMP.

### 3.2. Microwave-Assisted Synthesis of Magnetic Nanoparticles

Aqueous solutions of FeCl<sub>3</sub>·6H<sub>2</sub>O (0.4 M) and FeSO<sub>4</sub>·7H<sub>2</sub>O (0.2 M) were mixed together, after which a water solution of 2 M NaOH was added. The stirring was kept constant for 15 min. The solution was afterwards placed in a microwave oven (Anton Paar monowave 600, Graz, Austria) and irradiated at 100, 150, and 200 °C for 5 min under stirring. The obtained dark precipitates (Fe<sub>3</sub>O<sub>4</sub>) was separated from the suspensions by a magnet, washed several times with DI and dried at 80 °C for 2 h.

### 3.3. Synthesis of Fe<sub>3</sub>O<sub>4</sub>/SiO<sub>2</sub> Nanoparticles

Half a gram of dried magnetite particles were dispersed in a solution of ethanol, DI, and ammonia. The suspension was ultrasonicated for 15 min. After ultrasonication, TEOS was added dropwise to the solution with magnetite and stirred for 24 h. The TEOS:EtOH:DI:NH<sub>3</sub> molar ratio of the used chemicals was 1:100:32:0.003 [27]. The obtained particles (Fe<sub>3</sub>O<sub>4</sub>/SiO<sub>2</sub>) were then separated from the suspension with a magnet, washed several times with DI and dried at 40 °C for 3 h.

### 3.4. Microwave-Assisted Synthesis of Fe<sub>3</sub>O<sub>4</sub>/SiO<sub>2</sub>/TiO<sub>2</sub> Nanoparticles

Half a gram of dried Fe<sub>3</sub>O<sub>4</sub>/SiO<sub>2</sub> particles were dispersed in ethanol and ultrasonicated for 15 min. TiO<sub>2</sub> sol was prepared by mixing Pr-OH, AcAc, TIP, and 0.5 M HNO<sub>3</sub> in a TIP:PrOH:AcAc:HN molar ratio of 1:35:0.63:0.015 [28] and left covered until the next day. The next day, TiO<sub>2</sub> sol was added dropwise to the suspension with magnetic particles under vigorous stirring. The suspension was stirred for 15 min and transferred in a microwave oven at 200 °C for 10 min. The obtained Fe<sub>3</sub>O<sub>4</sub>/SiO<sub>2</sub>/TiO<sub>2</sub> nanocomposites were separated from the suspension with a magnet, washed several times with DI and dried at 60 °C for 3 h.

### 3.5. Materials Characterization

All the particles, i.e., Fe<sub>3</sub>O<sub>4</sub>, Fe<sub>3</sub>O<sub>4</sub>/SiO<sub>2</sub>, and Fe<sub>3</sub>O<sub>4</sub>/SiO<sub>2</sub>/TiO<sub>2</sub>, were characterized via vibrating-sample magnetometry (VSM), FTIR, XRD, and SEM.

VSM was performed using a Lake Shore Cryotronics vibrating sample magnetometer (Westerville, OH, USA). Hysteresis measurements were conducted in continuous acquisition mode with the maximum field of 20 kOe and a step size of 20 Oe.

FTIR measurements were performed using IRSpirit (Shimadzu, Tokyo, Japan) equipped with the single-reflection attenuated total reflectance (ATR) accessory in the wavenumber range of 400 to 4000 cm<sup>-1</sup>.

XRD was performed on XRD-6000 (Shimadzu, Tokyo, Japan) using CuKα radiation at an accelerating voltage of 40 kV and a current of 30 mA. All samples were analyzed in a 2θ range of 5°–75° in a continuous mode with a 0.02° 2θ step and a scan rate of 0.6 s.

SEM was conducted via SEM Tescan Vega III Easyprobe, with an accelerating voltage of 10 kV, equipped with secondary (SE) and backscattered electron (BSE) detectors (Tescan, Brno, Czech Republic).

### 3.6. Synergetic Adsorption and Photocatalytic Evaluation

The photocatalytic activity of the prepared magnetite-based magnetic nanocomposite synthesized at 100 °C was examined by the degradation of CIP as the selected micropollutant. Fifty milligrams of the photocatalyst were dispersed in a 100 cm<sup>3</sup> aqueous CIP solution, with a concentration of 10 mg dm<sup>-3</sup> irradiated by UV-A (365 nm) lamp (model UVAHAND LED; Dr. Hönle AG, München, Germany). The photocatalysis process was carried out in a round reactor made of borosilicate glass with a flat bottom, shown in Figure 11. The selected lamp was placed under the reactor at a distance of 10 cm, while stirring was provided from above with a polyamide stirring bar.

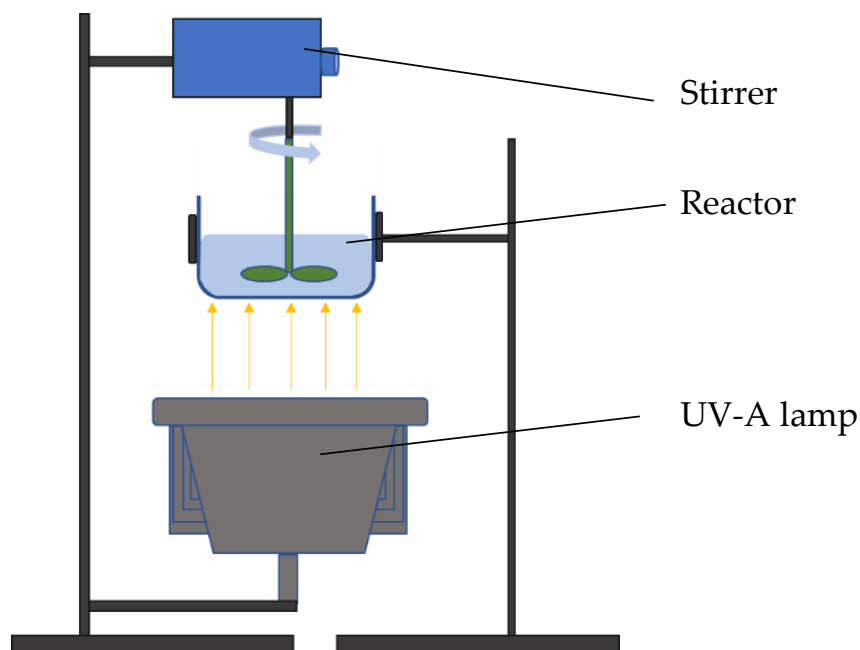


**Figure 11.** The reactor for photocatalytic measurements.

Before photocatalytic evaluation, adsorption tests were conducted by stirring 100 cm<sup>3</sup> of the aqueous CIP solution with the photocatalyst in the dark for 120 min. Based on the obtained results, the adsorption kinetics was evaluated.

The photolysis effect was also evaluated by stirring 100 cm<sup>3</sup> of the aqueous CIP solution for 120 min, while the solution was irradiated with a lamp without the photocatalyst in the reactor.

CIP degradation was followed as an absorbance decrease by UV/VIS spectrophotometry (Spekol 2000, Analytic Jena, Jena, Germany) at a wavelength of 273 nm. CIP can exist as a cation ( $pK_a$  lower than 5.90), a zwitterion ( $pK_a$  between 5.90 and 8.89), and an anion ( $pK_a$  above 8.89) under typical water pH conditions, as shown in Figure 12. Changing the pH values affected both the surface charge of the adsorbent and the degree of ionization. The electrostatic effects between the catalyst surface and the functional groups of the micropollutant at active sites of the catalyst were also affected by pH value. The efficiency of the catalyst at pH values lower than ~6 was reduced because of the repulsive effect between the positively charged catalyst surface and CIP. On the other hand, the efficiency at pH values higher than ~9 was reduced due to the electrostatic repulsion of negative charges of CIP and TiO<sub>2</sub> [54,55]. Based on all mentioned before, the pH of the CIP solution was kept at around 6.5.

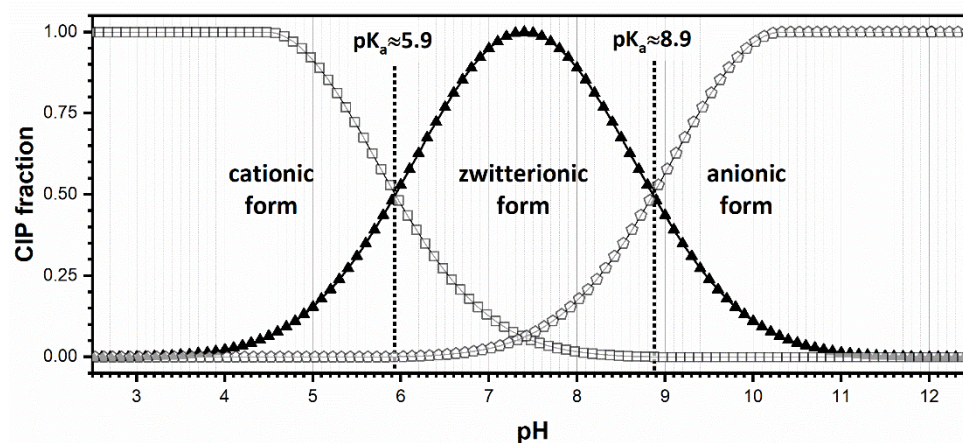


Figure 12. Molecular structure of CIP and its ionic forms as a function of pH and  $pK_a$  values [56].

#### 4. Conclusions

$Fe_3O_4/SiO_2/TiO_2$  nanocomposites were successfully prepared by microwave-assisted synthesis. The FTIR and XRD analysis confirmed the successful synthesis of a magnetic nanophotocatalyst. The magnetization curves showed that the obtained particles exhibited superparamagnetic behavior. The SEM analysis showed a disordered surface texture of the prepared magnetite particles. The presence of some agglomerates occurred due to the small size of particles and their magnetization. To address agglomeration issues, the use of a surfactant and a longer microwave irradiation with high stirring rates may prove beneficial.

Adsorption kinetic studies suggested that the adsorption of CIP on ternary core-shell  $Fe_3O_4/SiO_2/TiO_2$  nanocomposites might be controlled by the second-order model. The intraparticle diffusion plots indicated that multiple steps took place during the sorption process. The Boyd diagram showed that the inherent penetration along with the film penetration controlled the adsorption mechanism. The synergetic removal of CIP encompassed photolysis (without photocatalyst nanocomposites) degradation of around 40%, dark adsorption degradation of around 56% after 30 min, and photocatalytic degradation around 94% after 120 min of irradiation. The magnetic ternary core-shell  $Fe_3O_4/SiO_2/TiO_2$  catalyst featured high stability and good reusability under UV light irradiation. After three replications, the photodegradation efficiency of CIP decreased from 94.0% to 91.0%. The measurement of iron concentration in eluate confirmed that no leaching occurred during the photocatalytic examination.

Efficient photocatalyst separation by an external magnetic field will allow the reuse of core-shell nanocomposites in repeating processes of water purification.

**Author Contributions:** Conceptualization, I.G. and L.Ć.; methodology, I.G. and L.Ć.; formal analysis, I.G., V.M., I.P. and K.Z.; investigation, I.G., L.Ć., V.M., I.P. and D.L.; data curation, I.G., L.Ć., V.M., I.P. and K.Z.; writing—original draft preparation, I.G. and L.Ć.; writing—review and editing, L.Ć., D.L., V.M., I.P. and K.Z.; visualization, I.G., L.Ć. and V.M.; supervision, L.Ć.; project administration, L.Ć. and V.M.; funding acquisition, L.Ć. and V.M. All authors have read and agreed to the published version of the manuscript.

**Funding:** This work has been fully supported by Croatian Science Foundation under the projects IP-2016-06-6000: Monolithic and composite advanced ceramics for wear and corrosion protection (WECOR) and UIP-2019-04-2367: Surface limitations in preparing and infiltration of hard porous nanomaterial by soft or liquid precursors for performance enhancing (SLIPPERYSLOPE).

**Institutional Review Board Statement:** Not applicable.

**Informed Consent Statement:** Not applicable.

**Data Availability Statement:** Data sharing is not applicable to this article.

**Conflicts of Interest:** The authors declare no conflict of interest.

## References

1. Pati, S.S.; Kalyani, S.; Mahendran, V.; Philip, J. Microwave assisted synthesis of magnetite nanoparticles. *J. Nanosci. Nanotechnol.* **2014**, *14*, 5790–5797. [[CrossRef](#)]
2. Lininger, C.N.; Cama, C.A.; Takeuchi, K.J.; Marschlok, A.C.; Takeuchi, E.S.; West, A.C.; Hybertsen, M.S. Energetics of Lithium Insertion into Magnetite, Defective Magnetite, and Maghemite. *Chem. Mater.* **2018**, *30*, 7922–7937. [[CrossRef](#)]
3. Samrot, A.V.; Sahithya, C.S.; Selvarani, A.J.; Purayil, S.K.; Ponnaiah, P. A review on synthesis, characterization and potential biological applications of superparamagnetic iron oxide nanoparticles. *Curr. Res. Green Sustain. Chem.* **2021**, *4*, 100042. [[CrossRef](#)]
4. Kostyukhin, E.M.; Kustov, L.M. Microwave-assisted synthesis of magnetite nanoparticles possessing superior magnetic properties. *Mendeleev Commun.* **2018**, *28*, 559–561. [[CrossRef](#)]
5. Farahbakhsh, F.; Ahmadi, M.; Hekmatara, S.H.; Sabet, M.; Heydari-Bafrooei, E. Improvement of photocatalyst properties of magnetic NPs by new anionic surfactant. *Mater. Chem. Phys.* **2019**, *224*, 279–285. [[CrossRef](#)]
6. Patil, R.M.; Thorat, N.D.; Shete, P.B.; Bedge, P.A.; Gavde, S.; Joshi, M.G.; Tofail, S.A.M.; Bohara, R.A. Comprehensive cytotoxicity studies of superparamagnetic iron oxide nanoparticles. *Biochem. Biophys. Rep.* **2018**, *13*, 63–72. [[CrossRef](#)] [[PubMed](#)]
7. Aisida, S.O.; Akpa, P.A.; Ahmad, I.; Zhao, T.k.; Maaza, M.; Ezema, F.I. Bio-inspired encapsulation and functionalization of iron oxide nanoparticles for biomedical applications. *Eur. Polym. J.* **2020**, *122*, 109371. [[CrossRef](#)]
8. Lastovina, T.A.; Budnyk, A.P.; Kubrin, S.P.; Soldatov, A.V. Microwave-assisted synthesis of ultra-small iron oxide nanoparticles for biomedicine. *Mendeleev Commun.* **2018**, *28*, 167–169. [[CrossRef](#)]
9. Ling, D.; Lee, N.; Hyeon, T. Chemical synthesis and assembly of uniformly sized iron oxide nanoparticles for medical applications. *Acc. Chem. Res.* **2015**, *48*, 1276–1285. [[CrossRef](#)] [[PubMed](#)]
10. Ansari, L.; Malaek-Nikouei, B. Magnetic silica nanocomposites for magnetic hyperthermia applications. *Int. J. Hypertherm.* **2017**, *33*, 354–363. [[CrossRef](#)]
11. Li, S.S.; Li, W.J.; Jiang, T.J.; Liu, Z.G.; Chen, X.; Cong, H.P.; Liu, J.H.; Huang, Y.Y.; Li, L.N.; Huang, X.J. Iron Oxide with Different Crystal Phases ( $\alpha$ - and  $\gamma$ -Fe<sub>2</sub>O<sub>3</sub>) in Electroanalysis and Ultrasensitive and Selective Detection of Lead(II): An Advancing Approach Using XPS and EXAFS. *Anal. Chem.* **2016**, *88*, 906–914. [[CrossRef](#)]
12. Zeng, Z.; Zhao, H.; Wang, J.; Lv, P.; Zhang, T.; Xia, Q. Nanostructured Fe<sub>3</sub>O<sub>4</sub>@C as anode material for lithium-ion batteries. *J. Power Sources* **2014**, *248*, 15–21. [[CrossRef](#)]
13. Aisida, S.O.; Madubuonu, N.; Alnasir, M.H.; Ahmad, I.; Botha, S.; Maaza, M.; Ezema, F.I. Biogenic synthesis of iron oxide nanorods using Moringa oleifera leaf extract for antibacterial applications. *Appl. Nanosci.* **2020**, *10*, 305–315. [[CrossRef](#)]
14. Alzahrani, E. Photodegradation of Binary Azo Dyes Using Core-Shell Fe<sub>3</sub>O<sub>4</sub>/SiO<sub>2</sub>/TiO<sub>2</sub> Nanospheres. *Anal. Chem.* **2017**, *8*, 95–115. [[CrossRef](#)]
15. Brossault, D.F.F.; McCoy, T.M.; Routh, A.F. Self-assembly of TiO<sub>2</sub>/Fe<sub>3</sub>O<sub>4</sub>/SiO<sub>2</sub> microbeads: A green approach to produce magnetic photocatalysts. *J. Colloid Interface Sci.* **2021**, *584*, 779–788. [[CrossRef](#)] [[PubMed](#)]
16. Jiang, Q.; Huang, J.; Ma, B.; Yang, Z.; Zhang, T.; Wang, X. Recyclable, hierarchical hollow photocatalyst TiO<sub>2</sub>@SiO<sub>2</sub> composite microsphere realized by raspberry-like SiO<sub>2</sub>. *Colloids Surf. A Physicochem. Eng. Asp.* **2020**, *602*, 125112. [[CrossRef](#)]
17. Narzary, S.; Alamelu, K.; Raja, V.; Jaffar Ali, B.M. Visible light active, magnetically retrievable Fe<sub>3</sub>O<sub>4</sub>@SiO<sub>2</sub>@g-C<sub>3</sub>N<sub>4</sub>/TiO<sub>2</sub> nanocomposite as efficient photocatalyst for removal of dye pollutants. *J. Environ. Chem. Eng.* **2020**, *8*, 104373. [[CrossRef](#)]
18. Bo, Z.; Dong, R.; Jin, C.; Chen, Z. High photocatalytically active cocoons-like TiO<sub>2</sub>/SiO<sub>2</sub> synthesized by hydrothermal process and subsequent calcination at 900 °C. *Mater. Sci. Semicond. Process.* **2017**, *72*, 9–14. [[CrossRef](#)]
19. Ljubas, D.; Franzreb, M.; Hansen, H.C.B.; Weidler, P.G. Magnetizing of nano-materials on example of Degussa's P-25 TiO<sub>2</sub> photocatalyst: Synthesis of magnetic aggregates, characterization and possible use. *Sep. Purif. Technol.* **2014**, *136*, 274–285. [[CrossRef](#)]
20. Suwannaruang, T.; Kamonsuangkasem, K.; Kidkhunthod, P.; Chirawatkul, P.; Saiyasombat, C.; Chanlek, N.; Wantala, K. Influence of nitrogen content levels on structural properties and photocatalytic activities of nanorice-like N-doped TiO<sub>2</sub> with various calcination temperatures. *Mater. Res. Bull.* **2018**, *105*, 265–276. [[CrossRef](#)]
21. Sultana, S.; Amirbahman, A.; Tripp, C.P. A method to produce robust magnetic particles coated with TiO<sub>2</sub> nano particulates. *Appl. Catal. B Environ.* **2020**, *273*, 118935. [[CrossRef](#)]
22. Fernández, L.; Gamallo, M.; González-Gómez, M.A.; Vázquez-Vázquez, C.; Rivas, J.; Pintado, M.; Moreira, M.T. Insight into antibiotics removal: Exploring the photocatalytic performance of a Fe<sub>3</sub>O<sub>4</sub>/ZnO nanocomposite in a novel magnetic sequential batch reactor. *J. Environ. Manag.* **2019**, *237*, 595–608. [[CrossRef](#)]
23. Sohrabnezhad, S.; Pourahmad, A.; Karimi, M.F. Magnetite-metal organic framework core@shell for degradation of ampicillin antibiotic in aqueous solution. *J. Solid State Chem.* **2020**, *288*, 121420. [[CrossRef](#)]
24. Stan, M.; Lung, I.; Soran, M.L.; Leostean, C.; Popa, A.; Stefan, M.; Lazar, M.D.; Opris, O.; Silipas, T.D.; Porav, A.S. Removal of antibiotics from aqueous solutions by green synthesized magnetite nanoparticles with selected agro-waste extracts. *Process Saf. Environ. Prot.* **2017**, *107*, 357–372. [[CrossRef](#)]
25. Lastovina, T.A.; Budnyk, A.P.; Soldatov, M.A.; Rusalev, Y.V.; Guda, A.A.; Bogdan, A.S.; Soldatov, A.V. Microwave-assisted synthesis of magnetic iron oxide nanoparticles in oleylamine–oleic acid solutions. *Mendeleev Commun.* **2017**, *27*, 487–489. [[CrossRef](#)]
26. Ćurković, L.; Veseli, R.; Gabelica, I.; Žmak, I.; Ropuš, I.; Vukšić, M. A review of microwave-assisted sintering technique. *Trans. Famena* **2021**, *45*, 1–16. [[CrossRef](#)]

27. Li, C.; Wei, Y.; Liivat, A.; Zhu, Y.; Zhu, J. Microwave-solvothermal synthesis of Fe<sub>3</sub>O<sub>4</sub> magnetic nanoparticles. *Mater. Lett.* **2013**, *107*, 23–26. [[CrossRef](#)]
28. Kalan, R.E.; Yaparatan, S.; Amirbahman, A.; Tripp, C.P. P25 titanium dioxide coated magnetic particles: Preparation, characterization and photocatalytic activity. *Appl. Catal. B Environ.* **2016**, *187*, 249–258. [[CrossRef](#)]
29. Ćurković, L.; Ljubas, D.; Šegota, S.; Bačić, I. Photocatalytic degradation of Lissamine Green B dye by using nanostructured sol-gel TiO<sub>2</sub> films. *J. Alloys Compd.* **2014**, *604*, 309–316. [[CrossRef](#)]
30. Zhang, H.; Sun, S.; Ding, H.; Deng, T.; Wang, J. Effect of calcination temperature on the structure and properties of SiO<sub>2</sub> microspheres/nano-TiO<sub>2</sub> composites. *Mater. Sci. Semicond. Process.* **2020**, *115*, 105099. [[CrossRef](#)]
31. Balayeva, N.O.; Fleisc, M.; Bahnemann, D.W. Surface-Grafted WO<sub>3</sub>/TiO<sub>2</sub> Photocatalysts: Enhanced Visible-Light Activity towards Indoor Air Purification. *Catal. Today* **2018**, *313*, 63–71. [[CrossRef](#)]
32. Yu, H.; Irie, H.; Shimodaira, Y.; Hosogi, Y.; Kuroda, Y.; Miyauchi, M.; Hashimoto, K. An Efficient Visible-Light-Sensitive Fe(III)-Grafted TiO<sub>2</sub> Photocatalyst. *J. Phys. Chem. C* **2010**, *114*, 16481–16487. [[CrossRef](#)]
33. Ćizmić, M.; Ljubas, D.; Rožman, M.; Ašperger, D.; Ćurković, L.; Babić, S. Photocatalytic degradation of azithromycin by nanostructured TiO<sub>2</sub> film: Kinetics, degradation products, and toxicity. *Materials* **2019**, *12*, 873. [[CrossRef](#)]
34. Švigelj, Z.; Mandić, V.; Ćurković, L.; Biošić, M.; Žmak, I.; Gaborardi, M. Titania-Coated alumina foam photocatalyst for memantine degradation derived by replica method and sol-gel reaction. *Materials* **2020**, *13*, 227. [[CrossRef](#)]
35. Marinović, V.; Ćurković, L.; Ljubas, D. Effects of concentration and UV radiation wavelengths on photolytic and photocatalytic degradation of azo dyes aqueous solutions by sol-gel TiO<sub>2</sub> films. *Holist. Approach Environ.* **2016**, *7*, 3–14.
36. Wang, X.; Zhou, J.; Zhao, S.; Chen, X.; Yu, Y. Synergistic effect of adsorption and visible-light photocatalysis for organic pollutant removal over BiVO<sub>4</sub>/carbon sphere nanocomposites. *Appl. Surf. Sci.* **2018**, *453*, 394–404. [[CrossRef](#)]
37. Leong, K.H.; Aziz, A.A.; Kang, Y.L.; Goh, S.W.; Singh, K.V.; Sim, L.C.; Saravanan, P. Synergized mechanistic and solar photocatalysis features of N-TiO<sub>2</sub> functionalised activated carbon. *AIMS Mater. Sci.* **2017**, *4*, 800–813. [[CrossRef](#)]
38. Kaur, J.; Kaur, M. Facile fabrication of ternary nanocomposite of MgFe<sub>2</sub>O<sub>4</sub> TiO<sub>2</sub>@GO for synergistic adsorption and photocatalytic degradation studies. *Ceram. Int.* **2019**, *45*, 8646–8659. [[CrossRef](#)]
39. Huang, J.; Chen, W.; Yu, X.; Fu, X.; Zhu, Y.; Zhang, Y. Fabrication of a ternary BiOCl/CQDs/rGO photocatalyst: The roles of CQDs and rGO in adsorption-photocatalytic removal of ciprofloxacin. *Colloids Surf. A Physicochem. Eng. Asp.* **2020**, *597*, 124758. [[CrossRef](#)]
40. Li, Y.; Jian, L.J.; Li, X.; Liu, F.T.; Dong, X.F.; Wang, J.; Zhao, Y.; Wang, C.W. Excellent synergistic effect of adsorption and photocatalytic degradation from the novel Cu<sub>3</sub>SnS<sub>4</sub>@C nano-heterostructure. *React. Kinet. Mech. Catal.* **2020**, *131*, 997–1007. [[CrossRef](#)]
41. Feifel, S.C.; Lisdat, F. Silica nanoparticles for the layer-by-layer assembly of fully electro-active cytochrome *c* multilayers. *J. Nanobiotechnol.* **2011**, *9*, 1–12. [[CrossRef](#)]
42. Shah, A.H.; Rather, M.A. Effect of calcination temperature on the crystallite size, particle size and zeta potential of TiO<sub>2</sub> nanoparticles synthesized via polyol-mediated method. *Mater. Today Proc.* **2021**, *4*, 482–488. [[CrossRef](#)]
43. Rani, N.; Dehiya, B.S. Influence of anionic and non-ionic surfactants on the synthesis of core-shell Fe<sub>3</sub>O<sub>4</sub>@TiO<sub>2</sub> nanocomposite synthesized by hydrothermal method. *Ceram. Int.* **2020**, *46*, 23516–23525. [[CrossRef](#)]
44. Jin, S.; Park, B.C.; Ham, W.S.; Pan, L.; Kim, Y.K. Effect of the magnetic core size of amino-functionalized Fe<sub>3</sub>O<sub>4</sub>-mesoporous SiO<sub>2</sub> core-shell nanoparticles on the removal of heavy metal ions. *Colloids Surf. A Physicochem. Eng. Asp.* **2017**, *531*, 133–140. [[CrossRef](#)]
45. Favela-Camacho, S.E.; Samaniego-Benítez, E.J.; Godínez-García, A.; Avilés-Arellano, L.M.; Pérez-Robles, J.F. How to decrease the agglomeration of magnetite nanoparticles and increase their stability using surface properties. *Colloids Surf. A Physicochem. Eng. Asp.* **2019**, *574*, 29–35. [[CrossRef](#)]
46. Zheng, T.; Wang, Q.; Shi, Z.; Zhang, Z.; Ma, Y. Microwave regeneration of spent activated carbon for the treatment of ester-containing wastewater. *RSC Adv.* **2016**, *6*, 60815–60825. [[CrossRef](#)]
47. Lagergren, S.; Svenska, B.K. Zur theorie der sogenannten adsorption gelöster stoffe. *Z. Chem. Ind. Kolloide* **1898**, *24*, 1–39. [[CrossRef](#)]
48. Ho, Y.S.; McKay, G. Pseudo-second order model for sorption processes. *Process. Biochem.* **1999**, *34*, 451–465. [[CrossRef](#)]
49. Ho, Y.S.; McKay, G. Sorption of dye from aqueous solution by peat. *Chem. Eng. Sci.* **1998**, *70*, 115–124. [[CrossRef](#)]
50. Weber, W.J.; Morris, J.C. Kinetics of adsorption on carbon from solution. *J. Sanit. Eng. Div. Am. Soc. Civ. Eng.* **1963**, *89*, 31–60. [[CrossRef](#)]
51. Janoš, P.; Šmídová, V. Effects of surfactants on the adsorptive removal of basic dyes from water using an organomineral sorbent—Iron humate. *J. Colloid Interface Sci.* **2005**, *291*, 19–27. [[CrossRef](#)] [[PubMed](#)]
52. Sophia, A.C.; Lima, E.C. Removal of emerging contaminants from the environment by adsorption. *Ecotoxicol. Environ. Saf.* **2018**, *150*, 1–17. [[CrossRef](#)] [[PubMed](#)]

53. Ahmadi, M.; Ramezani Motlagh, H.; Jaafarzadeh, N.; Mostoufi, A.; Saeedi, R.; Barzegar, G.; Jorfi, S. Enhanced photocatalytic degradation of tetracycline and real pharmaceutical wastewater using MWCNT/TiO<sub>2</sub> nanocomposite. *J. Environ. Manage.* **2017**, *186*, 55–63. [[CrossRef](#)]
54. Malakootian, M.; Nasiri, A.; Amiri Gharaghani, M. Photocatalytic degradation of ciprofloxacin antibiotic by TiO<sub>2</sub> nanoparticles immobilized on a glass plate. *Chem. Eng. Commun.* **2020**, *207*, 56–72. [[CrossRef](#)]
55. Ji, H.; Wang, T.; Huang, T.; Lai, B.; Liu, W. Adsorptive removal of ciprofloxacin with different dissociated species onto titanate nanotubes. *J. Clean. Prod.* **2021**, *278*, 123924. [[CrossRef](#)]
56. Genç, N.; Dogan, E.C. Adsorption kinetics of the antibiotic ciprofloxacin on bentonite, activated carbon, zeolite, and pumice. *Desalin. Water Treat.* **2015**, *53*, 785–793. [[CrossRef](#)]